

Thermal biasing at the nanoscale

Artem O. Denisov,^{†,‡} Evgeny S. Tikhonov,^{†,‡} Stanislau U. Piatrusha,^{†,‡} Daniele Ercolani,[¶] Francesco Rossella,[¶] Mirko Rocci,[¶] Lucia Sorba,[¶] Stefano Roddaro,^{¶,§} and Vadim S. Khrapai^{*,†,‡}

[†]*Institute of Solid State Physics, Russian Academy of Sciences, 142432 Chernogolovka, Russian Federation*

[‡]*Moscow Institute of Physics and Technology, Dolgoprudny, 141700 Russian Federation*

[¶]*NEST, Istituto Nanoscienze CNR and Scuola Normale Superiore, Piazza S. Silvestro 12, I-56127 Pisa, Italy*

[§]*Department of Physics "E.Fermi", Universita di Pisa, Largo Pontecorvo 3, I-56127 Pisa, Italy*

E-mail: dick@issp.ac.ru

Abstract

We present an innovative strategy to control a thermal bias in nanoscale electronic conductors which is based on the contact heating scheme. This straightforward approach allows one to apply a known thermal bias across nanostructures directly through metallic leads, avoiding conventional substrate intermediation. We show, by using the average noise thermometry and local noise sensing technique in InAs nanowire-based devices, , that a nanoscale metallic constriction on a SiO₂ substrate acts like a diffusive conductor with negligible electron-phonon relaxation and non-ideal leads. The non-universal impact of the leads on the achieved thermal bias — which depends on their dimensions, shape and material composition — can be quantified via a proper design of the nanodevice. Our results are relevant for accurate thermoelectric or similar

measurements at nanoscale, allowing to reduce the issue of the thermal bias calibration to the knowledge of the heater resistance.

Introduction

Managing nanoscale electronic devices out of thermal equilibrium is an outstanding problem both from the fundamental^{1,2} and applied perspectives.³ Unlike cooling the electrons down by refrigeration,^{4,5} raising their temperature above the thermal bath is achieved easily by Joule heating of the whole device,⁶ of a part of it^{7–9} or of the nearby substrate.^{10–16} Accurate control of the generated thermal bias, which is an obvious prerequisite for a quantitative measurement in thermoelectric (TE) and other similar experiments,^{17,18} remains a separate complex problem.

Various non-equilibrium control tools are capable of measuring the temperature of the electronic^{4,7,8,19} and lattice sub-systems,²⁰ including spatially resolved^{9,21–23} and energy resolved^{24,25} approaches. However, the accuracy of the control is strongly outweighed by the tools' complexity. Moreover, the modeling of the heat balance at nanoscale is often not reliable, for the *a-priori* unknown electron-phonon coupling,¹⁹ thermal contact resistance^{10,26–29} and lattice thermal conductivity.^{27,30,31} For instance, as demonstrated recently by some of us, below ~ 40 K the electron and lattice systems are practically decoupled in InAs nanowires (NWs),^{8,32} emphasizing the importance of the leads for substrate heating approaches in this temperature range. Not to mention that the thermal bias calibration by means of the metallic resistance thermometry³³ loses its sensitivity within the residual resistance range at low temperatures. These obstacles are easily overcome using a contact heating scheme accompanied by a primary calibration of the thermal bias via noise thermometry.⁷ In this case, a nearly ideal thermal contact between the electronic systems of a uniform current biased metallic heater and the nano-device is achieved by an ohmic contact of negligible resistance. Recently, this approach was successfully applied to TE measurements in individual InAs

NWs, using a heater shaped in the form of a metallic diffusive constriction.³²

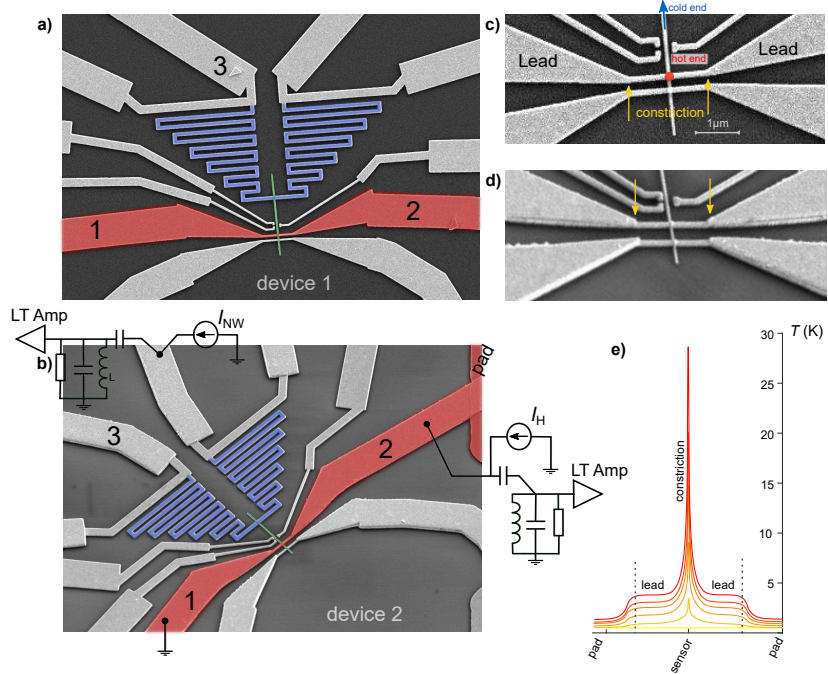


Figure 1: (a,b) SEM images of the studied devices: device 1 (D1, (a)) and device 2 (D2, (b)). The single InAs nanowire (NW, green) on SiO_2/Si substrate with Ni/Au nanostructure (gray, red, blue) deposited over it. The reddish strip between terminals 1 and 2 is the contact heater device under consideration. Terminal 2 is used to drive the heating current I_H and to measure the noise from the contact heater, while terminal 1 is connected to the common ground. Terminal 3 is connected to the NW through a meander-shaped strip (blue) and used to drive the current I_{NW} and measure the local noise. The shape of the blue strip is not intended to have an impact on the discussed experiments. The three side gates and all other unlabeled contacts were kept unconnected. (c,d) The magnified middle part of the heaters in D1 (c) and D2 (d). Short ($\sim 2\mu\text{m}$) Ni/Au constriction is connected to huge $\sim 160\mu\text{m}$ leads. Current I_H in the constriction heats up the 'hot end' of the NW, while the 'cold end' is kept thermalized at T_{bath} . The arrows mark the difference in the leads thickness between D1 and D2 (see text). (e) Numerically simulated spatial temperature profiles along the contact heater in D1 at different $|I_H| = 2\mu\text{A}, 1.4\mu\text{A}, 1.0\mu\text{A}, 0.6\mu\text{A}, 0.3\mu\text{A}, 0\mu\text{A}$

The question we answer in this work, is whether the accurate knowledge of the thermal bias across a nanostructure (the InAs NW on a SiO_2 substrate in our case) is possible without technical challenges imposed by the noise thermometry. We will show, that the universal expression for electron temperature in the center of a diffusive heater of resistance r at a

given bath temperature T_{bath} .^{34,35}

$$T = \sqrt{T_{\text{bath}}^2 + \frac{(rI_{\text{H}})^2}{4\mathcal{L}}}, \quad (1)$$

where $\mathcal{L} = \pi^2 k_{\text{B}}^2 / 3e^2$ is the Lorenz number, can be used to calibrate the thermal bias created by the constriction, without performing the noise measurements. A well-known issue in this case is the Joule heating of the metallic leads connecting the constriction to the external current source.³⁶ We demonstrate how to eliminate this problem by exploiting the heaters of different lead thicknesses and verify the idea using the local and average noise thermometry. The proposed strategy allows one to determine the thermal bias at nanoscale based solely on the knowledge of the heater resistance and, thus, appears to be commonly accessible to experimentalists working with thermal management at the nanoscale.

Devices

In our experiment we use two devices of identical planar architecture shown in the SEM images reported in Fig. 1a and Fig. 1b and marked as device 1 (D1) and device 2 (D2), respectively. Single InAs nanowire (see fabrication details in **”Materials and Methods”**), emphasized with green color, was deposited on the top of SiO_2/Si substrate. Colored with light-grey, are Ni/Au bilayers deposited by means of e-beam lithography on the substrate, which form ohmic contacts and side gates to the NW (the latter weren’t used throughout this work). In our measurements only the terminals numbered 1-3 were used while the others were floating. Reddish metallic strip between terminals 1 and 2, biased with current I_{H} , serves as the contact heater to the NW. The terminal 2 is connected to the DC external circuit and to the low-temperature amplifier for the average noise measurements, while the terminal 1 is kept grounded (see Fig. 1b). On the opposite side, each NW is connected via the terminal 3 and the bluish meander-shaped strip to the DC measurement circuit and another low-temperature amplifier, in this case for the local noise measurements⁸.

Important part of our devices is the constriction in the middle of the heater strip, see magnified SEM images in Fig. 1c and 1d. The constriction is represented by a $2\mu\text{m}$ long and narrow metallic wire, which smoothly evolves into the wide and macroscopically long ($\sim 160\mu\text{m}$) leads. Fig. 1c and 1d reveal a crucial difference between the two devices: D1 was passed through one-step lithography and, thus, a single $120\text{ nm}/10\text{ nm}$ thick Ni/Au layer appears, while two-step lithography for D2 provided a twice thicker metal in the leads area. This difference appears as an abrupt change in evaporated metal thickness marked by yellow arrows in Fig. 1d. Within each heater strip, the constriction serves as the main heater, whereas the remaining leads represent a non-ideal thermal reservoir. An example of a numerically simulated temperature profile along the heater strip is shown in Fig. 1e for different currents I_H , see section **Local vs average heater thermometry: impact of the non-ideal leads** for the details. Note that the maximum temperature is achieved in the center of the constriction, where the InAs NW connects to the heater via the ohmic contact of negligible electric and thermal resistance ($\sim 100\Omega$ vs a few $\text{k}\Omega$ resistance of the NW).

In the following, we discuss the measurements performed in the device D1, since there are no qualitative differences with the D2 case. The only exception is reported in section **Quantitative strategy for thermal biasing in linear response**, where we analyze the role of the leads thickness using both devices.

InAs NW as an energy preserving sensor

The goal of this section is to summarize the capabilities of a diffusive InAs NW as a sensor of the local temperature⁸ and the local energy distribution.²⁵ This is the only experimental section in which the NW is connected to the external current source and biased with the current I_{NW} , which flows between the terminals 3 and 1 in Fig. 1. We start from the characterization of the transport regime in the InAs NW measuring its shot noise at a bath temperature $T_{\text{bath}} = 4.2\text{ K}$. In Fig. 2a we plot the measured NW noise temperature $T_{\text{NW}} =$

$S_I R_{\text{NW}} / 4k_B$, where S_I is the noise spectral density and R_{NW} is the differential resistance of the NW as a function of I_{NW} , while $I_H = 0$.

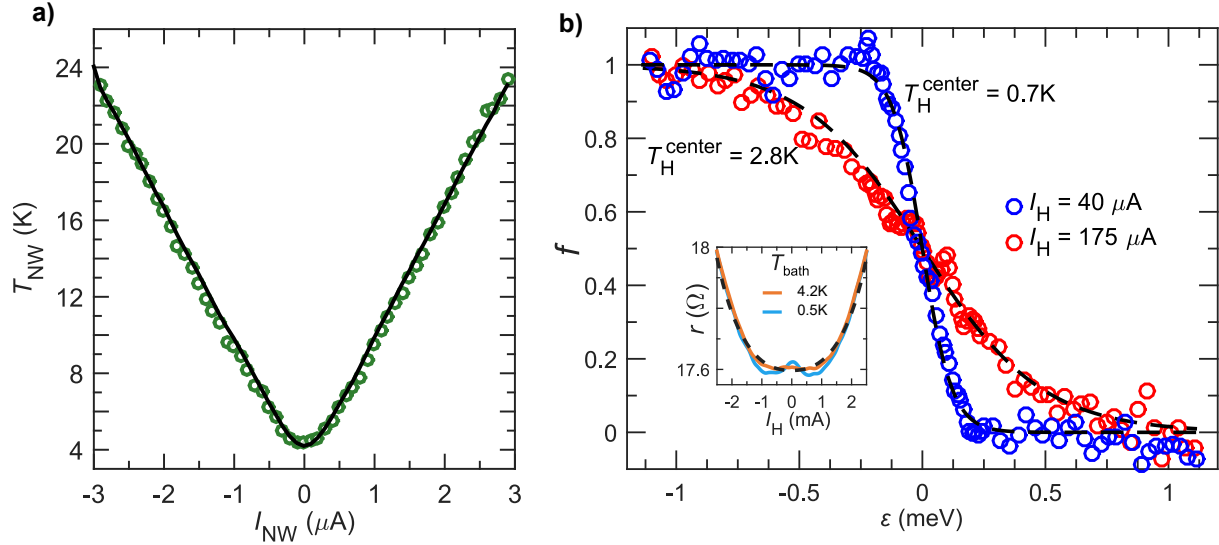


Figure 2: (a) The noise temperature of the NW as a function of I_{NW} at $I_H = 0$ and $T_{\text{bath}} = 4.2 \text{ K}$ (green symbols). Solid line is the shot-noise prediction with $F = 0.32$, which is close to the universal value for elastic diffusive conductor. (b) The electron energy distribution function in the center of metallic heater, measured via the shot-noise spectroscopy, see Ref. ²⁵ for details. The blue symbols are extracted from measurement at $I_H = 40 \mu\text{A}$, the red symbols from measurement at $I_H = 175 \mu\text{A}$. Dashed lines are equilibrium Fermi-Dirac distribution functions with specified temperatures T_H^{center} . The inset shows the nonlinear differential resistance r of the section between contacts 1 and 2 as a function of I_H at $T_{\text{bath}} = 4.2 \text{ K}$ (solid orange line) and $T_{\text{bath}} = 0.5 \text{ K}$ (solid blue line). The dashed line is the prediction with the conductivity correction proportional to $T^3 - T_{\text{bath}}^3$ (see text).

The crossover from the equilibrium Johnson-Nyquist noise $S_I = 4kT_{\text{bath}}/R_{\text{NW}}$ at $I_{\text{NW}} = 0$ to linear current dependence $S_I = 2eFI_{\text{NW}}$, where F is a Fano factor, is observed and persists up to $T_{\text{NW}} \approx 24 \text{ K}$ (symbols). The theoretical fit (solid line) meets experimental data at $F = 0.32$ which is very close to the universal value for diffusive conductors without electron-phonon relaxation $F = 1/3$.^{37,38} Thus, a quasiparticle energy is preserved along the NW, making it ideally suited for local noise sensing.⁸

As usual in the case of elastic diffusion,³⁷ the electronic energy distribution (EED) at a given location x along the NW, $f_\varepsilon(x)$, obeys the Laplace's equation $\partial^2 f_\varepsilon(x)/\partial x^2 = 0$. The solution is a linear combination of the EEDs $f_\varepsilon(0)$ and $f_\varepsilon(L)$ given by the external boundary

conditions at the two NW ends, respectively, $x = 0$ and $x = L$:

$$f_\varepsilon(x) = \left(1 - \frac{x}{L}\right)f_\varepsilon(0) + \frac{x}{L}f_\varepsilon(L) \quad (2)$$

The cold end of the InAs NW (connected to the terminal 3 at $x = 0$) is always kept in equilibrium with the corresponding EED $f_\varepsilon(0) = (1 + \exp(-\varepsilon/k_B T_{\text{bath}}))^{-1}$. In the following we focus on the experiments with a finite heater current I_H , thereby the second boundary condition in the eq. (2) is non-equilibrium. We evaluate the corresponding EED at $x = L$ by utilizing the energy resolved local noise spectroscopy.³⁹ In this experiment, performed with a separate device nominally identical to D2, both bias currents I_{NW} and I_H are finite. Also the I_H was chosen high enough, to avoid a problem with the noise analysis caused by a non-linearity of the NW resistance, see Ref.²⁵ for details. In Fig. 2b the measured $f_\varepsilon(L)$ is shown for two different I_H values along with the corresponding fits at the same $T_{\text{bath}} = 100 \text{ mK}$ (symbols and dashed lines, respectively). The measured $f_\varepsilon(L)$ is indistinguishable from the Fermi-Dirac EED $(1 + \exp(-\varepsilon/k_B T_{\text{H}}^{\text{center}}))^{-1}$, where $T_{\text{H}}^{\text{center}}$ is the temperature of the NW's hot end, which coincides with the local temperature in the center of the metallic heater constriction. Note that as soon as the EEDs at the NW's ends are known, there is a unique correspondence between the measured T_{NW} and the $T_{\text{H}}^{\text{center}}$, since $T_{\text{NW}} = \int L^{-1} dx \int f_\varepsilon(1 - f_\varepsilon) d\varepsilon$, see Ref.³⁷

The observation of the locally equilibrium EEDs in Fig. 2b implies strong thermalization of the charge carriers in the metallic heater constriction, even at relatively low temperatures of $T_{\text{bath}} = 100 \text{ mK}$ and $T_{\text{H}}^{\text{center}} = 0.7 \text{ K}$. This is in contrast to a naive expectation of a double-step EED generated by the current I_H .²⁴ We believe that the reason for such a strong thermalization is the electron-electron collisions in presence of a spin-flip scattering.⁴⁰⁻⁴² In our case such scattering is inevitable owing to the ferromagnetic Ni layer used in metalization. An independent signature of the spin-flip scattering comes from a zero-bias Kondo-like peak observed in a non-linear heater resistance in dependence of I_H at $T_{\text{bath}} = 0.5 \text{ K}$, see the blue

curve in inset of Fig.2b.

Local vs average heater thermometry: impact of the non-ideal leads

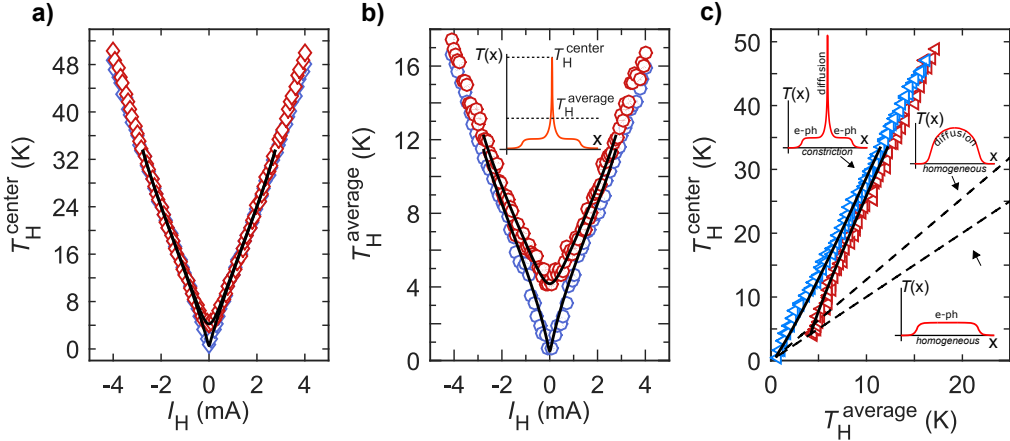


Figure 3: Local and average noise thermometry applied to the characterization of the temperature profile in the contact heater. (a) Measured local temperature in the center of Ni/Au constriction T_H^{center} at $T_{\text{bath}} = 0.5$ K (blue diamonds) and 4.2 K (red diamonds) along with the corresponding numerical simulations (black lines). (b) The same as (a) but for average temperature T_H^{average} of the heater. The inset shows an example of simulated spatial temperature profile along the heater $T(x)$ with marked T_H^{center} and T_H^{average} at $I_H = 2.5$ mA. (c) T_H^{center} plotted as a function of T_H^{average} . The experimental data from (a) and (b) are combined and shown by blue symbols ($T_{\text{bath}} = 0.5$ K) and red symbols ($T_{\text{bath}} = 4.2$ K). The solid lines are the result of numerical calculations based on heat balance equation (see text) for both bath temperatures. The dashed lines for $T_{\text{bath}} = 0.5$ K are predictions for the two limiting cases of the diffusion cooling and the electron-phonon cooling in a homogeneous conductor. The corresponding spatial temperature profiles $T(x)$ are shown in the nearby insets.

In this section we discuss the impact of the non-ideal leads of the metallic heater constriction on the thermal biasing. Here we supplement the local noise thermometry,⁸ which provides the knowledge of the temperature T_H^{center} at the NW contact position, i.e. at the center of the metallic constriction, with the conventional average noise thermometry.^{7,34,36} The latter approach is utilized via a measurement of the current noise of the heater strip as a whole, which is picked-up by the low-temperature amplifier at terminal 2. The measured signal in

this case is the average noise temperature T_H^{average} , which is given by the average of position-dependent heater temperature with the weight of local Joule heat.⁴³ The difference between the T_H^{center} and T_H^{average} , along with the spatial temperature distribution in the heater at $T_{\text{bath}} = 0.5 \text{ K}$ and $I_H = 2.5 \text{ mA}$, is demonstrated in the inset of Fig. 3b.

In Fig. 3a we plot the measured temperature T_H^{center} in the center of the metallic constriction against the bias current I_H at $T_{\text{bath}} = 0.5 \text{ K}$ and $T_{\text{bath}} = 4.2 \text{ K}$ (symbols). At $I_H = 0$, obviously, $T_H^{\text{center}} = T_{\text{bath}}$, while at increasing $|I_H|$ the measured temperature passes to the linear dependence up to $T_H^{\text{center}} \sim 50 \text{ K}$. As shown in Fig. 3b, the heater-averaged temperature T_H^{average} behaves similarly, also demonstrating a linear dependence on the bias current at large enough I_H (symbols). In this case, however, the measured temperature increase is considerably smaller. Such a strong discrepancy between the local and average temperatures highlights the main feature of our heater geometry, which is designed as a macroscopic metallic strip with a short constriction, see Fig. 1. In Fig. 3c we plot the T_H^{center} in dependence of the T_H^{average} (symbols), and compare the experimental results with the two limiting cases expected in a homogeneous conductor (dashed lines). Although the spatial temperature profiles are different in the case of a diffusion cooled conductor, sketched next to the upper dashed line, and in the case of the electron-phonon (e-ph) cooled conductor, sketched next to the lower dashed line, in both cases one obtains $T_H^{\text{center}}/T_H^{\text{average}} \approx 1$. By contrast, in our experiment $T_H^{\text{center}}/T_H^{\text{average}} \approx 3$, which is only possible given the constriction and the leads of the heater are in the regimes of diffusion cooling and e-ph cooling, respectively, the corresponding temperature profile is shown next to the experimental data in Fig. 3c.

The solid lines in Figs. 3a, 3b and 3c represent the results of numerical calculations used to fit the experimental data and characterize the parameters of the e-ph cooling in our devices. The underlying physics is captured by the heat balance equation:

$$-\nabla(\kappa_e \nabla T) = \frac{I_H^2}{\sigma_H A^2} - P_{\text{eph}}, \quad (3)$$

where $\kappa_e = \sigma_H \mathcal{L}T$ is the Wiedemann-Franz heat conduction of the electronic system, which is responsible for the diffusion cooling mechanism in the heater. The first term on the rhs of the eq. (3) accounts for the Joule heat production in the heater, whereas the second term stands for the e-ph cooling, both per unit volume. The best fits, capable to explain the data of Fig. 3 up to $|I_H| = 2.5$ mA are obtained with the following parameters. First, we assumed the power-law e-ph cooling $P_{\text{eph}} = \Sigma_{\text{eph}}(T^m - T_{\text{bath}}^m)$ with $\Sigma_{\text{eph}} = 4 \times 10^9$ W/m³K³ and $m = 3$. Note that this exponent is considerably smaller than the usual value of $m \approx 5$ ^{6,19} since we expect that the e-ph cooling is bottle-necked by the substrate.⁸ Second, we took the T -dependence of the heater conductivity into account via $\sigma_H = \sigma_H(T_{\text{bath}}) - \alpha(T^3 - T_{\text{bath}}^3)$, where $\sigma_H(T_{\text{bath}}) = 5.26 \times 10^7$ S/m is measured at $I_H = 0$ and $\alpha = 260$ S/mK³, which is consistent with the observed dependence of the total heater resistance at $T_{\text{bath}} = 4.2$ K, see the inset of Fig. 2b, and captures the main trend at $T_{\text{bath}} = 0.5$ K.

In a uniform conductor at $I_H = 0$ a small temperature difference $\delta T \ll T_{\text{bath}}$ decays exponentially in space. In this case the solution of the eq. (3) is $\delta T \propto \exp(-x/l_{\text{eph}})$, where $l_{\text{eph}} = \sqrt{\sigma_H \mathcal{L} / m \Sigma_{\text{eph}} T^{m-2}}$ is the e-ph relaxation length. For the above fit parameters we obtain $l_{\text{eph}} \approx 5$ μm and $l_{\text{eph}} \approx 14$ μm , respectively, at $T = 4.2$ K and $T = 0.5$ K in our Ni/Au metallic heaters. Experimentally, the elevated δT is achieved by means of the Joule heating. As seen from the eq. (3), the heating is much more efficient in the constriction, thanks to its drastically reduced cross-section area A , roughly by an order of magnitude as compared to the heater leads (see Fig. 1). In fact the linear in I_H trends of the T_H^{center} and T_H^{average} in Fig. 3 are qualitatively consistent with the simplified physical picture that our non-uniform heater consists of a 2 μm long ($\ll l_{\text{eph}}$) constriction cooled via diffusion of hot electrons in the ~ 160 μm long ($\gg l_{\text{eph}}$) well thermalized leads.

Quantitative strategy for thermal biasing in linear response

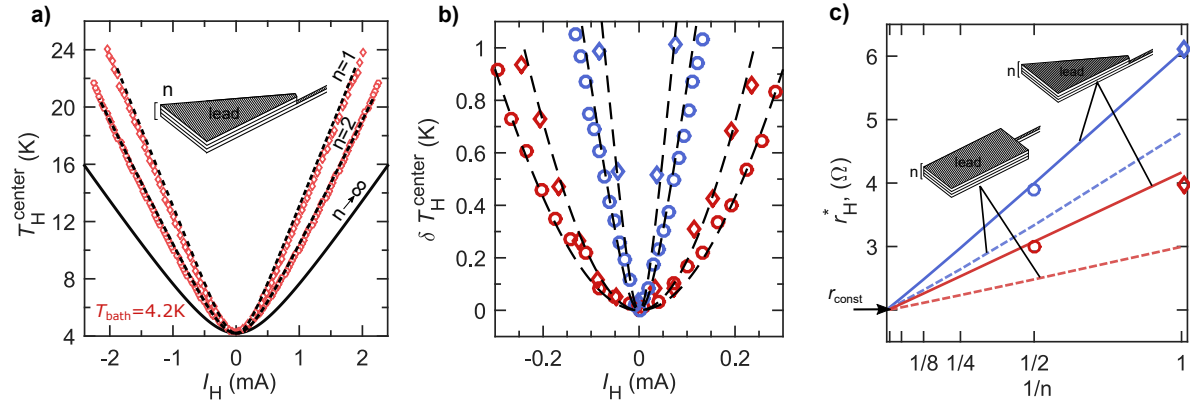


Figure 4: (a) The measured temperature in the center of the Ni/Au constriction T_H^{center} as a function of the heating current I_H at $T_{\text{bath}} = 4.2 \text{ K}$ for samples with the leads composed of $n = 1$ and $n = 2$ layers (red symbols, see text). The dashed lines are numerical calculations with corresponding n , while solid line is calculated for the case of ideal leads ($n \rightarrow \infty$). The inset depicts the schematic of the trapezoidal leads used in the experiment. (b) The similar measurements as (a) in a form of temperature increment $\delta T_H^{\text{center}} = T_H^{\text{center}} - T_{\text{bath}}$ at $T_{\text{bath}} = 0.5 \text{ K}$ (blue symbols) and 4.2 K (red symbols) for $n = 1$ (diamonds) and $n = 2$ (circles). The dashed lines are the fits with eq. (1) (see text). (c) The effective heater resistance r_H^* (see text) against the inverted number of layers in leads $1/n$. The theoretical predictions are built both for experimental lead geometry (solid lines) and for rectangular leads (dashed lines) at $T_{\text{bath}} = 0.5 \text{ K}$ (blue color) and 4.2 K (red color). The experimental data is shown as symbols of corresponding colors (diamonds for $n = 1$ and circles for $n = 2$). Note, that all theoretical predictions meet at $r_H^* = r_{\text{const}}$ when $n \rightarrow \infty$, where r_{const} is the resistance of the heater constriction.

In this section we investigate the impact of the thickness of the heater leads and propose a simple strategy to calibrate the thermal bias. In Fig. 4a we plot the temperature in the center of the heater constriction measured via local noise thermometry in dependence of I_H in two devices at $T_{\text{bath}} = 4.2 \text{ K}$ (symbols). The data clearly capture a systematic effect of the thickness of the metallic heater leads, which we express in terms of the number n of the 120 nm/10 nm thick Ni/Au bilayers. The T_H^{center} is considerably reduced in D2 ($n = 2$) as compared to the case of D1 ($n = 1$), which is perfectly consistent with the results of the

model calculation (dashed lines). The solid line in Fig. 4a also shows the calculation in the limit of $n \rightarrow \infty$, which corresponds to the idealized situation of the leads with zero electrical and heat resistances. Similar data in the form of $\delta T_H^{\text{center}} \equiv T_H^{\text{center}} - T_{\text{bath}}$ in dependence of I_H within a much narrower range are shown in Fig. 4b for the two values of T_{bath} used. The data of Fig. 4a and Fig. 4b demonstrate that the impact of non-ideal leads is visible both in the regime of strong and weak thermal biasing. Below we concentrate on the latter regime, $\delta T_H^{\text{center}} \ll T_{\text{bath}}$, which enables a remarkably simple calibration of the thermal bias.

As suggested by the eq. (1), we express the parabolic increase of the $\delta T_H^{\text{center}}$ as a function of heater current at small I_H as:

$$\delta T_H^{\text{center}} = \frac{(r_H^* I_H)^2}{8\mathcal{L}T_{\text{bath}}}, \quad (4)$$

where the effective heater resistance is denoted by r_H^* . Owing to the non-ideal leads of the heater, one expects that the actual value of r_H^* varies as a function of both T_{bath} and n in a given device. This is indeed observed in our experiment, as shown in Fig. 4c. The symbols in this plot show the values of r_H^* extracted from fitting the data of Fig. 4b with the eq. (1), as shown by the dashed lines in that figure. Remarkably, we observe that the experimental data in Fig. 4c follow a general linear in $1/n$ trend, predicted by the model calculations for the experimental geometry (solid lines and the sketch nearby). The observed linear increase of r_H^* with the inverse thickness of the heater leads ($1/n$) is also the case for a rectangular leads geometry (dashed lines and the sketch nearby), although the slope itself is non-universal.

The linear dependence of r_H^* on $1/n$ is easily understood. Thanks to a finite e-ph relaxation length in the leads, the effective resistance is that of the central part of the heater strip of the length corresponding to a few l_{eph} , which can be expressed as:

$$r_H^* = r_{\text{const}} + C \frac{\sigma_H^{-1} l_{\text{eph}}}{wt} + r_{\text{geom}}, \quad (5)$$

where r_{const} is the resistance of the constriction, $C \approx 3$ is a numerical factor, w and $t \propto n$ are,

respectively, the width and the thickness of the heater leads. The last term r_{geom} accounts for a temperature-independent geometrical factor of the leads, e.g., in our experiments the trapezoidal shaped leads result in $r_{\text{geom}} \approx 1.2 \Omega/n$.

As such, we propose the following strategy to calibrate the absolute value of the thermal bias at nanoscale:

- Design a device with at least two similar metallic heaters in the form of macroscopic leads and a constriction wire of the length $L \ll l_{\text{eph}}$ and the cross-section A much smaller than that of the leads. The thickness t of the metal in the leads should vary substantially between the heaters and be the same within the constrictions.
- Measure the TE voltage (or other thermal response) in the linear regime $V_{\text{TE}} \propto \delta T \propto (r_{\text{H}}^* I_{\text{H}})^2$ with different heaters.
- Using the equations (4-5) and the known resistance of the constriction $r_{\text{const}} = (L/A)\sigma_{\text{H}}^{-1}$ calibrate the effective heater resistance r_{H}^* and the thermal bias in the experiment in dependence of t^{-1} .

Summary

In summary, we achieved accurate thermal biasing of a nanoscale electronic device at low temperatures by means of a contact heating approach. Using the average noise thermometry and InAs NW-based local noise sensing we quantified the non-equilibrium electronic energy distribution and the temperature in the center of a metallic diffusive constriction in dependence of bias current. Numerical simulations allowed us to quantify the heat balance and the role of the non-ideal leads of the heater in the experiment. We presented a simple strategy how to design the metallic heaters capable of generating a predictable thermal bias at nanoscale.

Acknowledgement

We acknowledge valuable discussion with A.I. Kardakova and financial support from the SUPERTOP project, QUANTERA ERA-NET Cofound in Quantum Technologies and project xxx.

Materials and Methods

NW devices were fabricated starting from goldcatalyzed n-doped InAs NWs with typical length of $4\mu\text{m}$ and a diameter 85nm grown by chemical beam epitaxy.⁴⁴ The carrier density of the InAs NWs derived by field effect measurements is about $1 \times 10^{18}\text{cm}^{-3}$. Typical ohmic contact resistance in our devices is below 100Ω , whereas the NW resistance is about $10k\Omega$ per micrometer. The metallic nanostructures were realized by electron beam lithography (EBL) process involving two stages. First, 280 nm thick PMMA 950 K resist was spin-coated and followed by a soft-bake at 170°C for 90 sec. The sample was then exposed for e-beam (10kV) writing. Ni/Au (10/120 nm) was deposited via thermal evaporation on the e-beam written pattern for lift-off. Prior to the Ni/Au deposition, the NWs were passivated using an ammonium polysulfide $(\text{NH}_4)_2\text{S}_x$ solution, which ensured the formation of low-resistance ohmic contacts. Second, an additional standard EBL process was performed to achieve a precise overlay (with an accuracy $\sim 15\text{nm}$) and intentionally double the Ni/Au thickness, in the lead areas (see Fig. 1d).

We performed the measurements in two ^3He inserts, with the samples immersed in liquid (at $T_{bath} = 0.5\text{K}$) or in gas (at $T_{bath} = 4.2\text{K}$) and placed vertically face down. The shot noise spectral density was measured using home-made low-temperature amplifiers (LTamp) with a voltage gain of about 10 dB, input current noise of $\sim 10^{-27}\text{A}^2/\text{Hz}$ and dissipated power of $\sim 200\mu\text{W}$. We used a resonant tank circuit at the input of the LTamp, see the sketch in Fig. 1b, with a ground bypass capacitance of a coaxial cable and contact pads $\sim 40\text{pF}$, a hand-wound inductance of $\sim 5\mu\text{H}$ and a load resistance of $10k\Omega$. The output of the LTamp

was fed into the low noise 75 dB total voltage gain room temperature amplification stage followed by a hand-made analogue filter and a power detector. The setup has a bandwidth of $\Delta f \sim 0.5\text{MHz}$ around a center frequency of $\approx 11\text{MHz}$. A calibration was achieved by means of equilibrium Johnson-Nyquist noise thermometry. For this purpose we used a commercial pHEMT transistor connected in parallel with the device, that was depleted otherwise.

References

- (1) Dubi, Y.; Ventra, M. D. Thermoelectric Effects in Nanoscale Junctions. *Nano Letters* **2009**, *9*, 97–101.
- (2) Ye, L.; Zheng, X.; Yan, Y.; Di Ventra, M. Thermodynamic meaning of local temperature of nonequilibrium open quantum systems. *Phys. Rev. B* **2016**, *94*, 245105.
- (3) Snyder, G. J.; Toberer, E. S. Complex thermoelectric materials. *Nature Materials* **2008**, *7*, 105 EP –, Review Article.
- (4) Giazotto, F.; Heikkilä, T. T.; Luukanen, A.; Savin, A. M.; Pekola, J. P. Opportunities for mesoscopics in thermometry and refrigeration: Physics and applications. *Rev. Mod. Phys.* **2006**, *78*, 217–274.
- (5) Muhonen, J. T.; Meschke, M.; Pekola, J. P. Micrometre-scale refrigerators. *Reports on Progress in Physics* **2012**, *75*, 046501.
- (6) Roukes, M. L.; Freeman, M. R.; Germain, R. S.; Richardson, R. C.; Ketchen, M. B. Hot electrons and energy transport in metals at millikelvin temperatures. *Phys. Rev. Lett.* **1985**, *55*, 422–425.
- (7) Strunk, C.; Henny, M.; Schönenberger, C.; Neuttiens, G.; Van Haesendonck, C. Size Dependent Thermopower in Mesoscopic AuFe Wires. *Phys. Rev. Lett.* **1998**, *81*, 2982–2985.

(8) Tikhonov, E. S.; Shovkun, D. V.; Ercolani, D.; Rossella, F.; Rocci, M.; Sorba, L.; Roddaro, S.; Khrapai, V. S. Local noise in a diffusive conductor. *Scientific Reports* **2016**, *6*, 30621 EP –, Article.

(9) Menges, F.; Mensch, P.; Schmid, H.; Riel, H.; Stemmer, A.; Gotsmann, B. Temperature mapping of operating nanoscale devices by scanning probe thermometry. *Nature Communications* **2016**, *7*.

(10) Shi, L.; Li, D.; Yu, C.; Jang, W.; Kim, D.; Yao, Z.; Kim, P.; Majumdar, A. Measuring Thermal and Thermoelectric Properties of One-Dimensional Nanostructures Using a Microfabricated Device. *Journal of Heat Transfer* **2003**, *125*, 881.

(11) Zuev, Y. M.; Chang, W.; Kim, P. Thermoelectric and Magnetothermoelectric Transport Measurements of Graphene. *Phys. Rev. Lett.* **2009**, *102*, 096807.

(12) Zuev, Y. M.; Lee, J. S.; Galloy, C.; Park, H.; Kim, P. Diameter Dependence of the Transport Properties of Antimony Telluride Nanowires. *Nano Letters* **2010**, *10*, 3037–3040, PMID: 20698617.

(13) Wu, P. M.; Gooth, J.; Zianni, X.; Svensson, S. F.; Gluschke, J. G.; Dick, K. A.; Thelander, C.; Nielsch, K.; Linke, H. Large Thermoelectric Power Factor Enhancement Observed in InAs Nanowires. *Nano Letters* **2013**, *13*, 4080–4086, PMID: 23919739.

(14) Roddaro, S.; Ercolani, D.; Safeen, M. A.; Suomalainen, S.; Rossella, F.; Giazotto, F.; Sorba, L.; Beltram, F. Giant Thermovoltage in Single InAs Nanowire Field-Effect Transistors. *Nano Letters* **2013**, *13*, 3638–3642.

(15) Moon, J.; Kim, J.-H.; Chen, Z. C.; Xiang, J.; Chen, R. Gate-Modulated Thermoelectric Power Factor of Hole Gas in GeSi CoreShell Nanowires. *Nano Letters* **2013**, *13*, 1196–1202, PMID: 23394480.

(16) Chen, I.-J.; Burke, A.; Svilans, A.; Linke, H.; Thelander, C. Thermoelectric Power Factor Limit of a 1D Nanowire. *Phys. Rev. Lett.* **2018**, *120*, 177703.

(17) Seki, S.; Ideue, T.; Kubota, M.; Kozuka, Y.; Takagi, R.; Nakamura, M.; Kaneko, Y.; Kawasaki, M.; Tokura, Y. Thermal Generation of Spin Current in an Antiferromagnet. *Phys. Rev. Lett.* **2015**, *115*, 266601.

(18) Roura-Bas, P.; Arrachea, L.; Fradkin, E. Helical spin thermoelectrics controlled by a side-coupled magnetic quantum dot in the quantum spin Hall state. *Phys. Rev. B* **2018**, *98*, 195429.

(19) Wang, L. B.; Saira, O.-P.; Pekola, J. P. Fast thermometry with a proximity Josephson junction. *Applied Physics Letters* **2018**, *112*, 013105.

(20) Yazji, S.; Hoffman, E. A.; Ercolani, D.; Rossella, F.; Pitanti, A.; Cavalli, A.; Roddaro, S.; Abstreiter, G.; Sorba, L.; Zardo, I. Complete thermoelectric benchmarking of individual InSb nanowires using combined micro-Raman and electric transport analysis. *Nano Research* **2015**, *8*, 4048–4060.

(21) Doerk, G. S.; Carraro, C.; Maboudian, R. Single Nanowire Thermal Conductivity Measurements by Raman Thermography. *ACS Nano* **2010**, *4*, 4908–4914.

(22) Weng, Q.; Lin, K.-T.; Yoshida, K.; Nema, H.; Komiyama, S.; Kim, S.; Hirakawa, K.; Kajihara, Y. Near-Field Radiative Nanothermal Imaging of Nonuniform Joule Heating in Narrow Metal Wires. *Nano Letters* **2018**, *18*, 4220–4225.

(23) Weng, Q.; Komiyama, S.; Yang, L.; An, Z.; Chen, P.; Biehs, S.-A.; Kajihara, Y.; Lu, W. Imaging of nonlocal hot-electron energy dissipation via shot noise. *Science* **2018**, *360*, 775–778.

(24) Pothier, H.; Guéron, S.; Birge, N. O.; Esteve, D.; Devoret, M. H. Energy Distribution Function of Quasiparticles in Mesoscopic Wires. *Phys. Rev. Lett.* **1997**, *79*, 3490–3493.

(25) Piatrusha, S. U.; Khrapai, V. S. Measuring electron energy distribution by current fluctuations. 2017 International Conference on Noise and Fluctuations (ICNF). 2017; pp 1–4.

(26) Swinkels, M. Y.; van Delft, M. R.; Oliveira, D. S.; Cavalli, A.; Zardo, I.; van der Heijden, R. W.; Bakkers, E. P. A. M. Diameter dependence of the thermal conductivity of InAs nanowires. *Nanotechnology* **2015**, *26*, 385401.

(27) Zhou, F.; Moore, A. L.; Bolinsson, J.; Persson, A.; Fröberg, L.; Pettes, M. T.; Kong, H.; Rabenberg, L.; Caroff, P.; Stewart, D. A.; Mingo, N.; Dick, K. A.; Samuelson, L.; Linke, H.; Shi, L. Thermal conductivity of indium arsenide nanowires with wurtzite and zinc blende phases. *Phys. Rev. B* **2011**, *83*, 205416.

(28) Hochbaum, A. I.; Chen, R.; Delgado, R. D.; Liang, W.; Garnett, E. C.; Najarian, M.; Majumdar, A.; Yang, P. Enhanced thermoelectric performance of rough silicon nanowires. *Nature* **2008**, *451*, 163.

(29) Yazji, S.; Swinkels, M. Y.; Luca, M. D.; Hoffmann, E. A.; Ercolani, D.; Roddaro, S.; Abstreiter, G.; Sorba, L.; Bakkers, E. P. A. M.; Zardo, I. Assessing the thermoelectric properties of single InSb nanowires: the role of thermal contact resistance. *Semiconductor Science and Technology* **2016**, *31*, 064001.

(30) Li, D.; Wu, Y.; Kim, P.; Shi, L.; Yang, P.; Majumdar, A. Thermal conductivity of individual silicon nanowires. *Applied Physics Letters* **2003**, *83*, 2934–2936.

(31) Boukai, A. I.; Bunimovich, Y.; Tahir-Kheli, J.; Yu, J.-K.; Goddard III, W. A.; Heath, J. R. Silicon nanowires as efficient thermoelectric materials. *Nature* **2008**, *451*, 168 EP –.

(32) Tikhonov, E. S.; Shovkun, D. V.; Ercolani, D.; Rossella, F.; Rocci, M.; Sorba, L.; Roddaro, S.; Khrapai, V. S. Noise thermometry applied to thermoelectric measurements in InAs nanowires. *Semiconductor Science and Technology* **2016**, *31*, 104001.

(33) Tian, Y.; Sakr, M. R.; Kinder, J. M.; Liang, D.; MacDonald, M. J.; Qiu, R. L. J.; Gao, H.-J.; Gao, X. P. A. One-Dimensional Quantum Confinement Effect Modulated Thermoelectric Properties in InAs Nanowires. *Nano Letters* **2012**, *12*, 6492–6497, PMID: 23167670.

(34) Steinbach, A. H.; Martinis, J. M.; Devoret, M. H. Observation of Hot-Electron Shot Noise in a Metallic Resistor. *Phys. Rev. Lett.* **1996**, *76*, 3806–3809.

(35) Nagaev, K. E. Influence of electron-electron scattering on shot noise in diffusive contacts. *Phys. Rev. B* **1995**, *52*, 4740–4743.

(36) Henny, M.; Oberholzer, S.; Strunk, C.; Schönenberger, C. 1/3-shot-noise suppression in diffusive nanowires. *Phys. Rev. B* **1999**, *59*, 2871–2880.

(37) Nagaev, K. On the shot noise in dirty metal contacts. *Physics Letters A* **1992**, *169*, 103 – 107.

(38) Beenakker, C. W. J.; Büttiker, M. Suppression of shot noise in metallic diffusive conductors. *Phys. Rev. B* **1992**, *46*, 1889–1892.

(39) Gramespacher, T.; Büttiker, M. Local densities, distribution functions, and wavefunction correlations for spatially resolved shot noise at nanocontacts. *Phys. Rev. B* **1999**, *60*, 2375–2390.

(40) Kaminski, A.; Glazman, L. I. Electron Energy Relaxation in the Presence of Magnetic Impurities. *Phys. Rev. Lett.* **2001**, *86*, 2400–2403.

(41) Anthore, A.; Pierre, F.; Pothier, H.; Esteve, D. Magnetic-Field-Dependent Quasiparticle Energy Relaxation in Mesoscopic Wires. *Phys. Rev. Lett.* **2003**, *90*, 076806.

(42) Göppert, G.; Grabert, H. Nonequilibrium electron distribution in the presence of Kondo impurities. *Phys. Rev. B* **2001**, *64*, 033301.

(43) Piatrusha, S. U.; Khrapai, V. S.; Kvon, Z. D.; Mikhailov, N. N.; Dvoretsky, S. A.; Tikhonov, E. S. Edge states in lateral $p - n$ junctions in inverted-band HgTe quantum wells. *Phys. Rev. B* **2017**, *96*, 245417.

(44) Gomes, U. P.; Ercolani, D.; Zannier, V.; Beltram, F.; Sorba, L. Controlling the diameter distribution and density of InAs nanowires grown by Au-assisted methods. *Semiconductor Science and Technology* **2015**, *30*, 115012.